Functional and shunt states of bacteriorhodopsin resolved by 250 GHz dynamic nuclear polarization–enhanced solid-state NMR

Vikram S. Bajaj[a,1], Melody L. Mak-Jurkauskas[a,b], Marina Belenky[b], Judith Herzfeld[b], and Robert G. Griffin[a,2]

[a]Department of Chemistry and Francis Bitter Magnet Laboratory, Massachusetts Institute of Technology, Cambridge, MA 02139; and [b]Department of Chemistry, Brandeis University, Waltham, MA 02454

Edited by Brian M. Hoffman, Northwestern University, Evanston, IL, and approved April 13, 2009 (received for review January 27, 2009)

Observation and structural studies of reaction intermediates of proteins are challenging because of the mixtures of states usually present at low concentrations. Here, we use a 250 GHz gyrotron (cyclotron resonance maser) and cryogenic temperatures to perform high-frequency dynamic nuclear polarization (DNP) NMR experiments that enhance sensitivity in magic-angle spinning NMR spectra of cryo-trapped photocycle intermediates of bacteriorhodopsin (bR) by a factor of ≈90. Multidimensional spectroscopy of U-^{13}C,^{15}N-labeled samples resolved coexisting states and allowed chemical shift assignments in the retinylidene chromophore for several intermediates not observed previously. The correlation spectra reveal unexpected heterogeneity in dark-adapted bR, distortion in the K state, and, most importantly, 4 discrete L substates. Thermal relaxation of the mixture of L's showed that 3 of these substates revert to bR$_{568}$ and that only the 1 substate with both the strongest counterion and a fully relaxed 13-*cis* bond is functional. These definitive observations of functional and shunt states in the bR photocycle provide a preview of the mechanistic insights that will be accessible in membrane proteins via sensitivity-enhanced DNP NMR. These observations would have not been possible absent the signal enhancement available from DNP.

magic-angle spinning | photocycle intermediate | retinal protein | ion transport | DNP

Multidimensional magic-angle spinning (MAS) solid-state NMR is a general tool in structural studies of membrane proteins that are inaccessible to crystallography and solution-state NMR, as demonstrated by recent successful applications (1–3). But the sensitivity of these experiments is low, which becomes a significant problem when multidimensional experiments are needed to characterize systems of higher molecular weight. The sensitivity deficit is even more acute when NMR signals are further divided among multiple states, as is often the case for trapped reaction intermediates. Consequently, a 1–2 order of magnitude enhancement of NMR sensitivity is essential for applications of multidimensional MAS NMR methods to studies of reaction intermediates of membrane proteins.

One approach to improving the sensitivity of NMR is dynamic nuclear polarization (DNP), in which the ≈660-fold greater spin polarization of unpaired electrons in a paramagnetically doped glassy matrix is transferred to nuclei before an NMR experiment (4). Here, we demonstrate that high-frequency DNP by using a stable, high-power 250 GHz microwave source (5) and an efficient, nonperturbing biradical polarizing agent (6, 7), is a potentially general approach for biological MAS NMR. A 43-fold signal enhancement from DNP, combined with operation at 90 K, yields an overall 90-fold signal enhancement over previous experiments at 183 K (8). The resulting ≈8,100-fold savings in acquisition time permits 2-dimensional (2D) resolution of signals from mixtures of reaction intermediates that would be impossible to observe absent the enhancement available from DNP.

In bacteriorhodopsin (bR), 7 transmembrane helices surround a transport channel in which the Schiff base (SB) formed between retinal and lysine 216 (Fig. 1) provides the binding site for a labile proton. The counterion of the protonated SB comprises a hydrogen-bonded complex (9, 10) of polar side chains and several water molecules (11).

Absorption of a visible photon by the retinylidene chromophore initiates the photocycle

$$\begin{aligned} bR_{555} \rightleftarrows bR_{568} \xrightarrow{h\nu} J_{625} \rightarrow K_{590} \rightarrow L_{550} \xrightarrow{-H^+} M_{o\ 412} \\ \rightarrow M_{n\ 412} \xrightarrow{+H^+} N_{520} \rightarrow O_{640} \rightarrow bR_{568} \end{aligned} \quad [1]$$

in which the vectoriality of the pump is effected by a switch in connectivity of the SB from the extracellular side to the cytoplasmic side between the early and late M states, here designated M_o and M_n. Because isomerization of the chromophore occurs at the beginning of the photocycle (bR$_{568}$ to J) but the chromophore connectivity does not change until the middle of the photocycle, the details of the structural rearrangements occurring in the early photocycle intermediates (namely K and L) are fundamental to the control of vectoriality.

To apply MAS NMR to bR photocycle intermediates, a sample of bR$_{568}$ is irradiated in situ with laser light, and the resulting mixture of states is cryostabilized for data acquisition. The population of a desired intermediate can be favored by manipulating the temperature and wavelength during irradiation; however, the result is generally a mixture of bR$_{568}$ together with various intermediates. In such cases, a distinct advantage of NMR over diffraction is that signals from multiple species usually can be distinguished, because the chemical shifts depend on the local conformation and interactions. This is particularly so when there is sufficient signal to acquire multidimensional spectra.

Here, we report DNP-enhanced 2D MAS NMR spectra of bR intermediates acquired from U-^{13}C,^{15}N-labeled samples. The resolution afforded by chemical shift dispersion in the 2D MAS spectra of the cryogenically trapped photocycle intermediates allows us to identify cross-peaks belonging to unreacted bR$_{568}$, as well as several other components. There was evidence of

Author contributions: J.H. and R.G.G. designed research; V.S.B., M.L.M.-J., and M.B. performed research; V.S.B., M.L.M.-J., J.H., and R.G.G. analyzed data; and V.S.B., M.L.M.-J., J.H., and R.G.G. wrote the paper.

The authors declare no conflict of interest.

This article is a PNAS Direct Submission.

[1]Present address: Department of Chemistry, University of California, Berkeley, CA 94720.

[2]To whom correspondence should be addressed. E-mail: rgg@mit.edu.

This article contains supporting information online at www.pnas.org/cgi/content/full/0900908106/DCSupplemental.

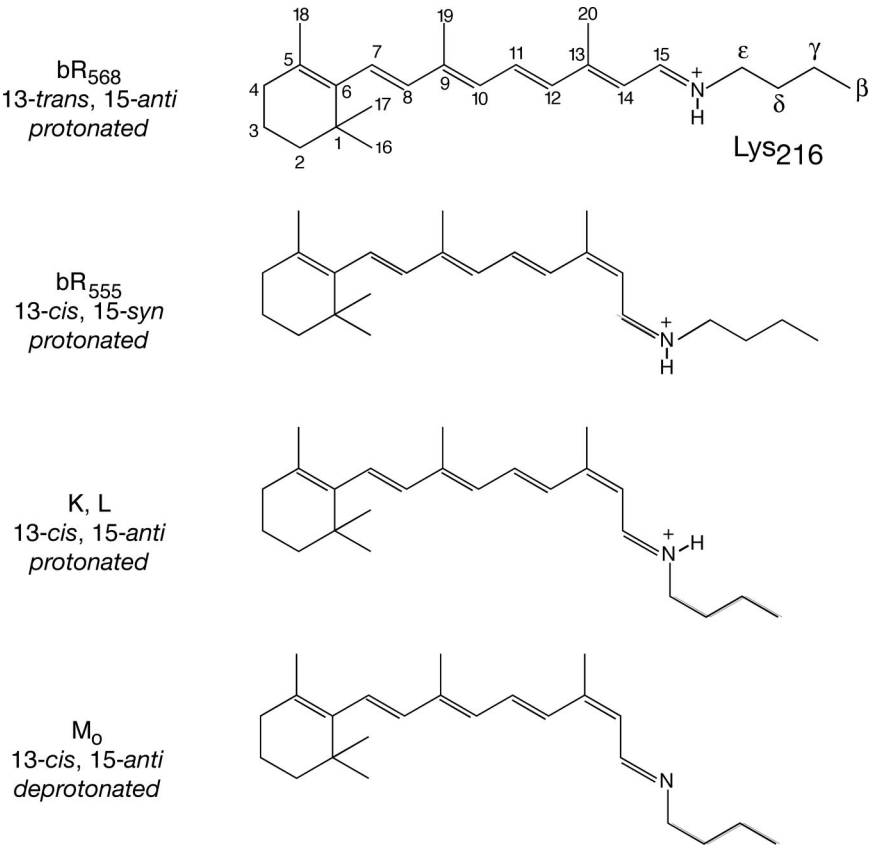

Fig. 1. The isomeric forms of the retinal chromophore in bR_{568}, bR_{555}, K–M_O. Note that the ^{15}N of the SB is protonated in all forms except M_O.

multiple intermediates in our previous 1-dimensional (1D) spectra (12, 13); however, the signal-to-noise ratio in the DNP-enhanced spectra and the 2D resolution presented here provide additional convincing support for their presence. For example, the 2D spectra reveal unexpected heterogeneity in dark-adapted bR, distortion in the K state and, most importantly, 4 discrete L substates. Temperature-dependent studies indicate that only one of these L substates is involved in ion translocation, whereas the other three are shunts that return to bR_{568}. The functional L state is distinguished from the shunt states by a very strong counterion interaction and planarization of the chromophore around the isomerized C13=C14 bond, contrary to crystallographic analysis (14). The finding that at least one of these features is absent from each of the shunt states suggests that they are difficult to achieve in the energy landscape of this part of the photocycle.

Results

Previous studies of bR intermediates were designed to probe structural rearrangements early in the photocycle, when the absorbed energy is still relatively localized in the active site. Changes can be deduced by monitoring chemical shifts, which also need to be assigned for eventual direct measurement of structural parameters. Our approach, using the pulse sequence shown in Fig. S1, entails (*i*) continuous irradiation of the electron resonance spectrum with 250-GHz microwaves; (*ii*) frequency-selective heteronuclear magnetization transfer (15) from the SB ^{15}N ($^{15}N\zeta$ of K216) to the C15 of retinal or the $^{13}C\varepsilon$ of K216, with the results shown in Fig. 2, and; (*iii*) further homonuclear polarization transfer (16–18) along the retinal polyene in the former case or along the K216 side chain in the latter case, with the results shown in Figs. 3 and 4, respectively.

Because of the extended topology of the chromophore, these experiments involve polarization transfer across several ^{13}C–^{13}C bonds and distribution of the SB magnetization across ≈7 ^{13}C sites in a single experiment, with polarization transfer efficiencies of <5% in the worst case. Because of the simul-

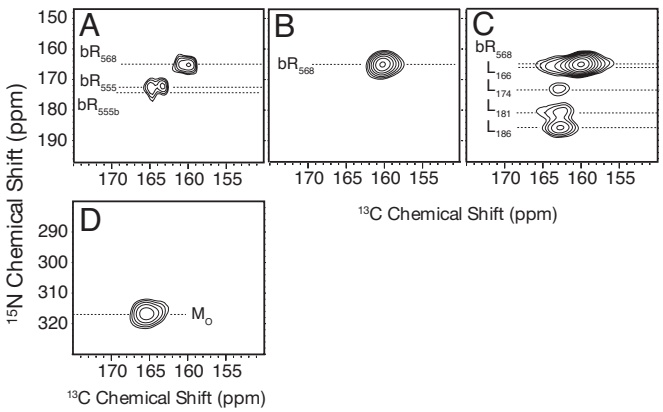

Fig. 2. $^{15}N\zeta$-$^{13}C15$ correlation experiments provide assignments of the retinal-C15 resonance in each state: dark-adapted (*A*); light-adapted (*B*), 4 L's with residual bR_{568} (*C*), and M_o (*D*). Note the downfield ^{15}N shifts observed in the L spectrum. The temperature and wavelength of the light used for preparation of each intermediate is as follows: (*A*) the dark-adapted state (bR_{555} and bR_{568}) obtained by room temperature equilibration in the dark; (*B*) the light-adapted state (bR_{568}) accumulated by 532 nm irradiation of (*A*) at 275 K; (*C*) a mixture of 4 L states, with bR_{568} accumulated by 640 nm irradiation of (*B*) at 150 K; and (*D*) the early M intermediate accumulated by 532 nm irradiation of (*B*) at 210 K. After accumulation, all of the intermediates were cooled to 90 K for data acquisition in the dark.

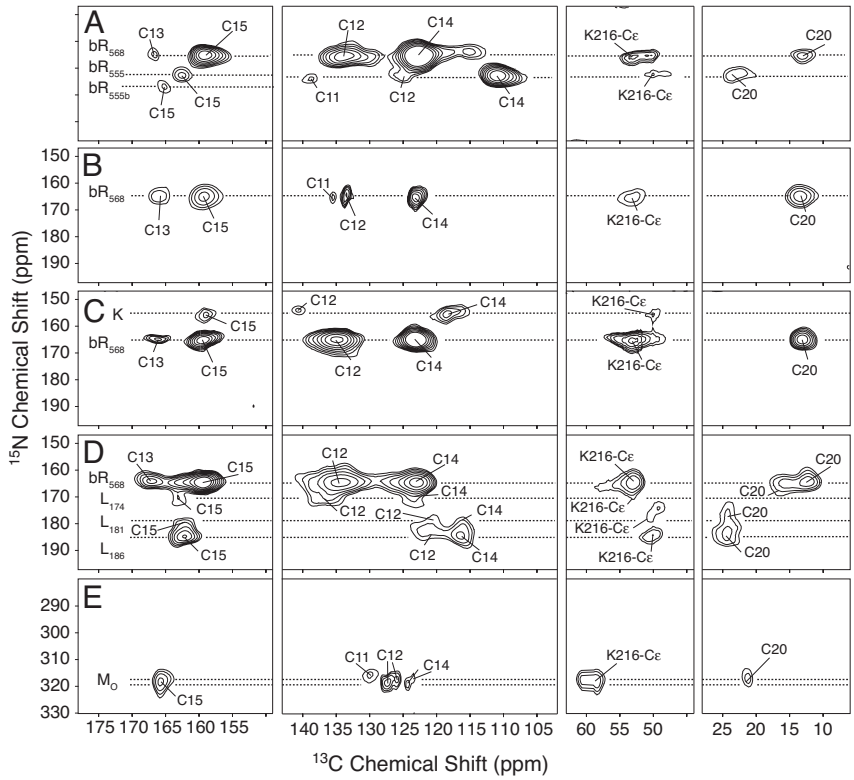

Fig. 3. $^{15}N\zeta$-$^{13}C15$-^{13}Cx correlation spectra that trace the connectivity of resonances in the retinylidene chromophore of bR in the dark-adapted state (*A*), the light-adapted state (*B*), the K state with residual bR_{568} (*C*), the L states with residual bR_{568} (*D*), and the M_o state with its deprotonated SB (*E*). Conditions are as specified for Fig. 2.

taneous presence of multiple photocycle intermediates, minor components of the mixture are further diluted by a factor of 2–20. Nevertheless, 2D spectra can be recorded in 12–48 h for all photocycle intermediates of bR, because of the large signal enhancement provided by low-temperature DNP. Thus, we detect single cross-peaks that correspond to single sites at an effective molecular weight of ≈660 kDa (see *Discussion*).

As shown in Figs. 2, 3, and 4, the ^{15}N SB chemical shift is exquisitely sensitive to its environment (19) and permits resolution of ^{13}C-^{15}N cross-peaks arising from the various intermediates. Additional homonuclear mixing, via either C15 or Cε, allows the observation of further heteronuclear correlations. Here, we obtain 9 or 10 chemical shift assignments for each intermediate (as tabulated in Tables S1 and S2). The ^{13}C assignments are based on the relative intensities of the cross-peaks and the expected chemical shift range for each site. Note that the cross-peak intensities are reduced when the polarization of the SB nitrogen is dispersed to more ^{13}C's (compare Figs. 3 and 4 vs. Fig. 2).

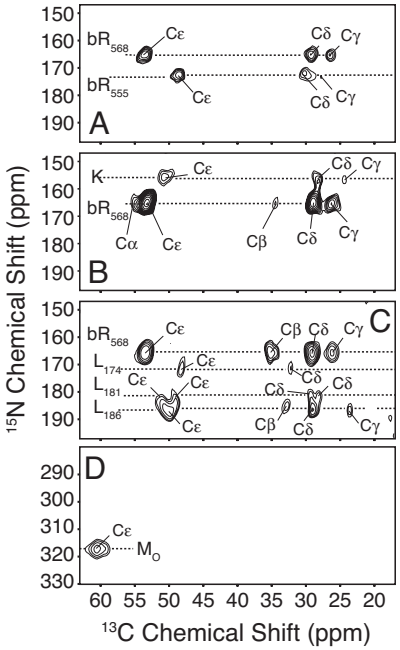

Fig. 4. $^{15}N\zeta$-$^{13}C\varepsilon$ correlation experiments in the dark-adapted state (*A*), the K intermediate with residual bR_{568} (*B*), the L intermediate with residual bR_{568} (*C*), and the M_o state (*D*). Conditions are as specified for Fig. 2.

Discussion

Multiplicity in Photocycle Intermediates. Examining the spectra in detail, we find single ^{15}N-^{13}C cross-peaks for each carbon atom in the light-adapted (Fig. 3*B*), K (Fig. 3*C*), and M_o (Fig. 3*E*) states. In contrast, the spectra of the dark-adapted (Figs. 2*A* and 3*A*) and L (Figs. 2*C* and 3*D*) states show heterogeneity. Dark adaptation is generally considered to involve the equilibration between all-*trans*, 15-*anti* bR_{568} and 13-*cis*,15-*syn* bR_{555}, and in 1D ^{15}N spectra we observe 2 lines in the 40:60 intensity ratio (19, 20) generally assigned to these species, with ^{15}N shifts that reflect 2 distinct environments for the SB. However, the stronger signals shown in Fig. 2*A* clearly indicate multiple ^{15}N-^{13}C cross-peaks for each species in the ^{13}C dimension. For the less-shielded SB (bR_{555}), the additional $^{15}N\zeta$-$^{13}C15$ splitting is particularly evident and indicates a well defined chromophore isomerization with an intensity ratio of ≈2:1 (5). We have not previously observed

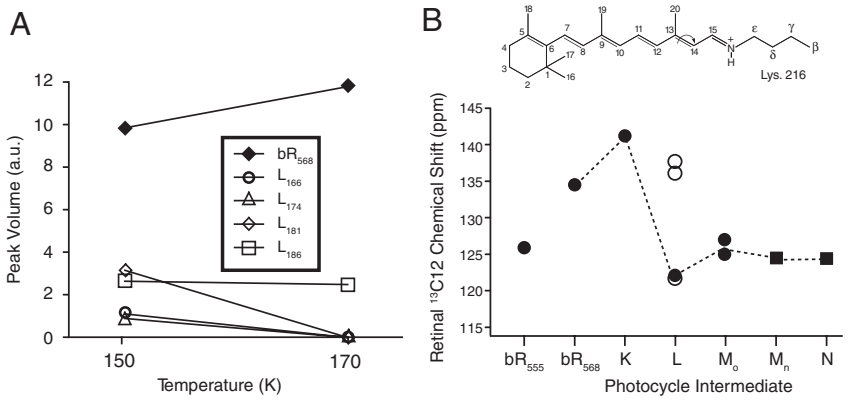

Fig. 5. Populations and ^{13}C12 chemical shifts of L substrates. (*A*) Volumes of the ^{15}Nζ-C15 peaks of the mixture formed by direct red light irradiation of bR_{568} at 150 K and of the mixture formed by subsequent thermal relaxation at 170 K. All L's except L_{186} revert to bR_{568} and thus are shunt states. Note that because cross-polarization efficiencies vary among the different intermediates, the intensity changes are nonstoichiometric. (*B*) Evolution of the retinal ^{13}C12 chemical shift through the various photocycle intermediates. Filled symbols represent functional states, and open symbols represent shunt (i.e., L_{166}, L_{174}, and L_{181}) states. The squares represent data from previous work (12, 28). Note that the steric interactions at C12 that are typical of the middle and late photocycle are achieved already in the functional form of L.

these splittings because of the limited resolution in 1D spectra. The splitting in both the bR_{555} and bR_{568} components of the dark-adapted mixture indicates that each represents at least 2 slightly different conformations in the neighborhood of the SB linkage. In contrast, these 4 lines coalesce to a single homogeneous species in the functional bR_{568} obtained after light adaptation (Figs. 2*B* and 3*B*).

Until recently, L was considered a well defined conformational intermediate; however, a recent deconvolution of time-resolved optical spectra suggested the presence of at least 2 substates (21), and our own recent 1D DNP solid-state NMR spectra identified 4 substates, 3 observed directly and 1 inferred from changes in bR_{568} intensity on generation of L (19). The latter is now clearly resolved (in Figs. 2*C* and 3*D*), because its C15 chemical shift differs from that of bR_{568}. Overall, the manifold of distinct ^{15}N-^{13}C cross-peaks suggests an ensemble of well defined L substates rather than a conformationally disordered state. When this 150 K mixture of substates (each identified by a subscript with its ^{15}N chemical shift) is warmed to 170 K, we find that the L_{186} signal persists and the signals from the other 3 L substates decrease whereas the bR_{568} signal grows (as shown in Fig. 5*A*). Thus, we conclude that the L_{166}, L_{174}, and L_{181} states contribute to the L-to-bR back-reaction first detected by low-temperature optical studies (22, 23) and recently confirmed by IR spectroscopy (24). However, because the persistent L_{186} relaxes to M at still-higher temperatures, we can confidently conclude that this is the functional L (19).

Development of Retinal Torsion in the Early Intermediates. Several retinal chemical shifts are particularly informative, because their relationship to specific structural parameters is well understood and the changes in the chemical shifts are not subtle. The ^{15}N chemical shifts of the SB in K and L indicate that the electrostatic interaction of the SB with its counterion in bR_{568} ($\approx$165 ppm) is broken in K ($\approx$155 ppm), but an exceptionally strong counterion interaction is established as the photocycle progresses to L_{186} (186 ppm) (19). These large changes, -10 ppm from bR_{568} to K and then + 30 ppm from K to L_{186}, are highly informative and support earlier evidence that electrostatic steering is important in driving the photocycle forward (25, 26).

Correlated changes are found in the C12 and C20 chemical shifts that reflect steric interactions with C15. In the planar 13-*trans* configuration, the proximity of the protons on C15 and C20 drives electrons toward those 2 carbons, increasing their shielding. Similarly, in the planar 13-*cis* configuration, the proximity of the protons on C15 and C12 increases shielding on those 2 carbons. This effect has been observed in comparisons of bR_{568} with bR_{555} (27), M_o, M_n (12), and N (28). Unfortunately, however, the C20 signal is not always sufficiently intense for detection here, and the C15 chemical shift is subject to additional effects.

However, C12 tells an interesting story (Fig. 5*B*). The relatively deshielded C12 signals in K ($\approx$140.7 ppm) in L_{166} and L_{174} ($\approx$137.0 ppm) indicate little steric interaction with C15 in these intermediates, suggesting that at least 1 of the 3 bonds between C12 and C15 is rotated from the fully planar 13-*cis* conformation, so that the protons of the 2 carbons are not pointing directly at one another. Conversely, the more shielded C12 in L_{181} and L_{186} ($\approx$120.4 ppm) suggests planarization around the *cis* C13=C14 bond comparable to that seen in subsequent intermediates ($\approx$125 ppm). (The only alternative source of shielding would be steric interactions with the protein; however, the crystal structures show no amino acid residues close enough to C12 to be responsible for the shielding.) The present results for K and L are consistent with earlier indications that single-bond torsion in the K intermediate is primarily around the C14–C15 bond and that double-bond torsion in the L intermediate is primarily around the C15=N bond (19). At the same time, the present results are inconsistent with the C13=C14 dihedral twist and the C12–C13=C14 bond angle expansion inferred for the L intermediate from analysis of x-ray diffraction data for mixtures of L and bR_{568} at 170K (14).

We should note that of the 3 crystal structures reported for the L intermediate (14, 29, 30), the 2 latest show the SB NH vector pointing either toward the cytoplasmic side of the membrane (29) or toward the extracellular side (14). The divergence in this essential detail may be related to the assumption in these crystallographic analyses that a single L conformation is present. But we find that shunt L states coexist with the functional L state $<$170 K in the native membrane, and it is possible that the temperature for relaxation of the shunt L states is higher in 3-dimensional crystals.

The cytoplasmic orientation of the SB NH vector in L is strongly favored in quantum mechanics/molecular mechanics (QM/MM) simulations. Three different potential pathways were initially identified for proton transfer from the SB to Asp-85 on the extracellular side (31, 32). Further simulations (32), stimulated in part by our 1D NMR data (12, 13, 19), suggest the presence of a low-energy conformer in which a water molecule bridges the protonated SB of the twisted chromophore and the carboxylate group of the proton acceptor Asp-85. These features

are consistent with the earlier NMR indications of double-bond torsion and a relatively strong SB interaction (13, 20) that we are now able to assign specifically to the functional form of L.

Dynamic Nuclear Polarization. The present results demonstrate that MAS NMR, in combination with low-temperature DNP, is sufficiently sensitive and specific to probe a mixture of intermediates of an effectively ≈33-kDa protein (26 kDa protein and 6.6 kDa accompanying lipids), yielding "snapshots" of the functional cycle. The enhanced sensitivity also facilitates the chemical shift assignments necessary for direct structural measurements. The spectra clearly show multiple L states and allow us to differentiate between the 1 substate that is functional and the 3 substates that are shunts. Experiments currently in progress should allow us to determine the subtle structural features of these intermediates that store and direct energy in the ion pump cycle. Furthermore, recent extensions of DNP instrumentation to 460 GHz (700 MHz ^{1}H) (33) will facilitate applications in systems requiring greater chemical shift resolution. Finally, recent and ongoing experimental improvements, such as lower temperatures (34, 35), better polarizing agents (36), and deuteration, should increase the efficiency and general applicability of the DNP process, allowing extension of the already important capabilities of DNP to a variety of new applications.

Materials and Methods

Sample Preparation. Uniformly ^{13}C,^{15}N-labeled peptone for the culture medium of *Halobacterium salinarum* was obtained from the anaerobic acid hydrolysis of *Methylophilus methylotrophus* grown on ^{13}C-labeled methanol and ^{15}N-labeled ammonium sulfate. The purple membranes were isolated according to the method of Oesterhelt and Stoeckenius (37), and washed with 40:60 vol/vol mixtures of 300 mM guanidine hydrochloride (pH 10) and d8-glycerol (vol/vol, for cryoprotection) containing 15 mM TOTAPOL (1-(2,2,6,6,-tetramethyl-1-oxyl-4-piperidinyl)oxy-3-(2,2,6,6-tetramethyl-1-oxy-4-oioeridinyl)amino-propan-2-ol), a nonperturbing biradical polarizing agent consisting of 2 TEMPO (2,2,6,6-tetramethylpiperidine-*N*-oxyl) moieties for DNP (7). A 57 μL sample was loaded into a 4 mm rotor made from a single-crystal sapphire rotor that was transparent at both optical and millimeter-wave frequencies.

Accumulation of Different Photocycle Intermediates. An optical fiber in the probe delivered green light (532 nm from a Coherent Verdi 6W DPSS laser) or red light (640 nm from a Coherent 599 dye laser pumped by the DPSS laser) to the spinning sample as needed. bR was dark-adapted by several hours of equilibration in the dark at room temperature and then light-adapted by green light at 273 K. Different photocycle intermediates were accumulated by illumination of light-adapted bR as follows:

K: green light at 90 K
L's: red light at 150 K
M_o: green light at 210 K.

Subsequently, NMR spectra of the accumulated intermediates were recorded in the dark at 90 K. Data acquisition at this low temperature also attenuated spin-lattice relaxation processes that otherwise compete with polarization transfer. IR light was used to monitor the MAS frequency to avoid interference with the preparation of photocycle intermediates or perturbation of the trapped photocycle intermediates. Cryogenic temperatures were achieved by using cooled dry nitrogen gas to drive MAS. Nitrogen gas was cooled by a pressurized heat exchanger immersed in liquid nitrogen and then delivered to the stator by transfer lines equipped with integral heaters and calibrated resistive temperature sensors for feedback regulation of the temperature (LakeShore Cryotronics). Temperatures reported here were measured in the sample chamber by using a Fabry-Perot interferometric thermometer (FISO Technologies), which is insensitive to magnetic and radiofrequency fields.

DNP/NMR Spectroscopy. All spectra were obtained on a home-built DNP spectrometer operating at a field of 9 T (250 GHz e^- and 380 MHz ^{1}H frequencies). A 250 GHz gyrotron produced high-power CW microwaves. The triple-resonance custom-designed probe used in the experiments also was equipped with a wave guide and a multimode optical fiber for delivery of microwave and laser light, respectively, to the sample. Detailed descriptions of the cryogenic MAS probe, microwave delivery to the sample, and the radiofrequency circuit are available elsewhere (38). Photointermediates were generated at the appropriate temperature, and the spectra were recorded at 90 K.

The pulse sequence used is shown in Fig. S1. Microwave radiation was applied continuously. After ^{1}H-^{15}N cross-polarization, the SB resonances were selected by a soft, band-selective ^{15}N pulse from the "E" family of selective excitation pulses optimized for solid-state NMR (39). Signals corresponding to the SB were along the *z*-axis, and all other signals were allowed to dephase. After rotation to the transverse plane, the ^{15}N magnetization arising from the SB resonances evolved under the ^{15}N chemical shift during t_1 and then was transferred selectively to retinal-C15 or K216-Cε by spectrally induced filtering in combination with cross-polarization (15). The ^{15}N and ^{13}C fields were chosen to provide spectrally selective, chemical-shift–dependent transfer to either directly bonded carbon, and a ramp of 5–6% in the ^{13}C radiofrequency field resulted in quasi-adiabatic transfer with improved efficiency. After an optional t_2 evolution period under the ^{13}C chemical shift, further correlations were established by homonuclear mixing by using proton-driven spin diffusion with a rotary resonance recoupling field (40) or radiofrequency-driven recoupling (17).

ACKNOWLEDGMENTS. We thank Drs. Jagadishwar Sirigiri and Richard J. Temkin for invaluable assistance, advice, and technical support. This work was supported by National Institute of Biomedical Imaging and Bioengineering of the National Institutes of Health Grants EB-001960, EB-002804, EB002026, and EB-001035. V.S.B. is a PGS Fellow of the Natural Sciences and Engineering Research Council of Canada. V.S.B. acknowledges the support of a postgraduate fellowship from the Natural Sciences and Engineering Research Council of Canada.

1. Jaroniec CP, et al. (2004) High-resolution molecular structure of a peptide in an amyloid fibril determined by magic-angle spinning NMR spectroscopy. *Proc Natl Acad Sci USA* 101:711–716.
2. Lange A, et al. (2006) Toxin-induced conformational changes in a potassium channel revealed by solid-state NMR. *Nature* 440:959–962.
3. Castellani F, et al. (2002) Structure of a protein determined by solid-state magic-angle-spinning NMR spectroscopy. *Nature* 420:98–102.
4. Carver TR, Slichter CP (1953) Polarization of nuclear spins in metals. *Phys Rev* 92:212–213.
5. Bajaj VS, et al. (2007) 250-GHz CW gyrotron oscillator for dynamic nuclear polarization in biological solid-state NMR. *J Magn Reson* 189:251–279.
6. Hu K-N, Yu H-H, Swager TM, Griffin RG (2004) Dynamic nuclear polarization with biradicals. *J Am Chem Soc* 126:10844–10845.
7. Song C, Hu K-N, Swager TM, Griffin RG (2006) TOTAPOL: A biradical polarizing agent for dynamic nuclear polarization experiments in aqueous media. *J Am Chem Soc* 128:11385–11390.
8. Lansing JC, et al. (2002) Chromophore distortions in the bacteriorhodopsin photocycle: Evolution of the H-C14–C15-H dihedral angle measured by solid-state NMR. *Biochemistry* 41:431–438.
9. de Groot HJM, Harbison GS, Herzfeld J, Griffin RG (1989) Nuclear magnetic resonance study of the Schiff base in bacteriorhodopsin: Counterion effects on the N-15 shift anisotropy. *Biochemistry* 28:3346–3353.
10. de Groot HJM, et al. (1990) Solid-state C-13 and N-15 NMR study of the low-pH forms of bacteriorhodopsin. *Biochemistry* 29:6873–6883.
11. Luecke H, Schobert B, Richter HT, Cartailler JP, Lanyi JK (1999) Structure of bacteriorhodopsin at 1.55-angstrom resolution. *J Mol Biol* 291:899–911.
12. Hu JG, et al. (1998) Early and late M intermediates in the bacteriorhodopsin photocycle: A solid-state NMR study. *Biochemistry* 37:8088–8096.
13. Hu JG, Sun BQ, Petkova AT, Griffin RG, Herzfeld J (1997) The predischarge chromophore in bacteriorhodopsin: A N-15 solid-state NMR study of the L photointermediate. *Biochemistry* 36:9316–9322.
14. Lanyi JK, Schobert B (2007) Structural changes in the L photointermediate of bacteriorhodopsin. *J Mol Biol* 365:1379–1392.
15. Baldus M, Petkova AT, Herzfeld J, Griffin RG (1998) Cross-polarization in the tilted frame: Assignment and spectral simplification in heteronuclear spin systems. *Mol Phys* 95:1197–1207.
16. Bennett AE, et al. (1998) Homonuclear radiofrequency-driven recoupling in rotating solids. *J Chem Phys* 108:9463–9479.
17. Bennett AE, Ok JH, Griffin RG, Vega S (1992) Chemical-shift correlation spectroscopy in rotating solids: Radiofrequency-driven dipolar recoupling and longitudinal exchange. *J Chem Phys* 96:8624–8627.
18. Takegoshi K, Nakamura S, Terao T (2001) C-13-H-1 dipolar-assisted rotational resonance in magic-angle spinning NMR. *Chem Phys Lett* 344:631–637.
19. Mak-Jurkauskas ML, et al. (2008) Energy transformations early in the bacteriorhodopsin photocycle revealed by DNP-enhanced solid-state NMR. *Proc Natl Acad Sci USA* 105:883–888.
20. Harbison GS, Herzfeld J, Griffin RG (1983) Solid-state N-15 nuclear magnetic resonance study of the Schiff base in bacteriorhodopsin. *Biochemistry* 22:1–5.
21. Zimanyi L, Saltiel J, Brown LS, Lanyi JK (2006) A priori resolution of the intermediate spectra in the bacteriorhodopsin photocycle: The time evolution of the L spectrum revealed. *J Phys Chem A* 110:2318–2321.

22. Litvin FF, Balashov SP, Sineshchekov VA (1975) Investigation of primary photochemical conversions of bacteriorhodopsin in purple membranes and cells of halobacterium-halobium by low-temperature spectrophotometry method. *Bioorganicheskaya Khimiya* 1:1767–1777.
23. Kalisky O, Ottolenghi M, Honig B, Korenstein R (1981) Environmental effects on the formation and photoreaction of the M412 photoproduction of bacteriorhodopsin: Implication for the mechanism of proton pumping. *Biochemistry* 20:649–655.
24. Dioumaev AK, Lanyi JK (2007) Bacteriorhodopsin photocycle at cryogenic temperatures reveals distributed barriers of conformational substates. *Proc Natl Acad Sci USA* 104:9621–9626.
25. Herzfeld J, Lansing JC (2002) Magnetic resonance studies of the bacteriorhodopsin pump cycle. *Annu Rev Biophys Biomol Struct* 31:73–95.
26. Hatcher ME, et al. (2002) Control of the pump cycle in bacteriorhodopsin: Mechanisms elucidated by solid-state NMR of the D85N mutant. *Biophys J* 82:1017–1029.
27. Harbison GS, et al. (1984) Dark-adapted bacteriorhodopsin contains 13-*cis*, 15-*syn*, and all-*trans*,15-*anti* retinal Schiff bases. *Proc Natl Acad Sci USA* 81:1706–1709.
28. Lakshmi KV, et al. (1994) Solid-state C-13-NMR and N-15-NMR investigations of the N intermediate of bacteriorhodopsin. *Biochemistry* 33:8853–8857.
29. Kouyama T, Nishikawa T, Tokuhisa T, Okumura H (2004) Crystal structure of the L intermediate of bacteriorhodopsin: Evidence for vertical translocation of a water molecule during the proton pumping cycle. *J Mol Biol* 335:531–546.
30. Lanyi JK, Schobert B (2003) Mechanism of proton transport in bacteriorhodopsin from crystallographic structures of the K–M-1, M-2, and M-2 ′ intermediates of the photocycle. *J Mol Biol* 328:439–450.
31. Bondar AN, Elstner M, Suhai S, Smith JC, Fischer S (2004) Mechanism of primary proton transfer in bacteriorhodopsin. *Structure* 12:1281–1288.
32. Bondar AN, Baudry J, Suhai S, Fischer S, Smith JC (2008) Key role of active-site water molecules in bacteriorhodopsin proton-transfer reactions. *J Phys Chem B* 112:14729–14741.
33. Hornstein MK, Bajaj VS, Griffin RG, Temkin RJ (2006) Continuous-wave operation of a 460-GHz second harmonic gyrotron oscillator. *IEEE Trans Plasma Sci* 34:524–533.
34. Hall DA, et al. (1997) Polarization-enhanced NMR spectroscopy of biomolecules in frozen solution. *Science* 276:930–932.
35. Thurber K, Tycko R (2008) Biomolecular solid-state NMR with magic-angle spinning at 25 K. *J Magn Reson* 195:179–186.
36. Matsuki Y, et al. (2009) Dynamic nuclear polarization using a rigid biradical. *Angewandte Chemie*, in press.
37. Oesterhelt D, Stoeckenius W (1974) Isolation of the cell membrane of Halobacterium halobium and its fractionation into red and purple membrane. *Methods Enzymol* 31:667–678.
38. Barnes AB, et al. (2009) Cryogenic sample-exchange NMR probe for magic-angle spinning dynamic nuclear polarization. *J Magn Reson* 198:261–270.
39. Veshtort M, Griffin RG (2004) High-performance selective excitation pulses for solid- and liquid-state NMR spectroscopy. *Chemphyschem* 5:834–850.
40. Oas TG, Griffin RG, Levitt MH (1988) Rotary resonance recoupling of dipolar interactions in solid- state nuclear magnetic-resonance spectroscopy. *J Chem Phys* 89:692–695.